JOURNAL OF AEROSPACE COMPUTING, INFORMATION, AND COMMUNICATION
Vol. 6, March 2009

Optimization of Nonlinear Lateral Characteristic of Lifting-Body Type Reentry Vehicle

Shinkyu Jeong*, Kunihiro Suzuki†, and Shigeru Obayashi‡
Tohoku University, Sendai, Miyagi, 980-8577, Japan

and

Mitsuru Kurita§
Japan Aerospace Exploration Agency, Chofu, Tokyo, 182-8622, Japan

DOI: 10.2514/1.36302

The nonlinear lateral characteristics of a lifting-body type reentry vehicle were improved by applying efficient optimization techniques to determine the optimum configuration. First, the causes for the nonlinear lateral characteristics were investigated by computational fluid dynamics analysis. The results indicated that fins mounted on the Japan Aerospace Exploration Agency's baseline lifting-body configuration cause unsymmetrical development of vortices and result in nonlinear lateral characteristics. An efficient optimization algorithm, called efficient global optimization for multiobjective problems, was adopted to improve these nonlinear lateral characteristics. Efficient global optimization for multiobjective problems predicts potential optimum solutions based on the probability estimated by the Kriging model. The computational time for optimization was markedly reduced owing to use of the Kriging model. Further investigations were also performed to determine the effects of the upswept upper-aft and swept-back fin angles. The results indicated that the swept-back fin angle is an important factor controlling the lateral characteristics of the lifting-body type reentry vehicle.

Nomenclature

$Cn\beta_{1\text{deg}}$, $Cl\beta_{1\text{deg}}$	derivative of yawing and rolling moment
$Cn\beta_*$, $Cl\beta_*$	yawing and rolling moment at a sideslip angle of * deg.
L/D	lift-to-drag ratio
s	estimated uncertainty from the Kriging model
$\hat{y}$	estimated objective function value from the Kriging model
α	angle of attack, deg.
β	sideslip angle, deg.
Φ	standard distribution
ϕ	standard normal density

Received 21 December 2007; revision received 19 August 2008; accepted for publication 24 November 2008.

* Associate Professor, Institute of Fluid Science, 2-1-1 Katahira, Aoba-ku, AIAA Member.
† Master course student, Institute of Fluid Science, 2-1-1 Katahira, Aoba-ku.
‡ Professor, Institute of Fluid Science, 2-1-1 Katahira, Aoba-ku, AIAA Associate Member.
§ Researcher, Institute of Aerospace Technology, 7-44-1 Jindaiji-Higashi, AIAA Member.

I. Introduction

REUSABLE space transportation systems have been developed to replace nonreusable launch systems. JAXA (Japan Aerospace Exploration Agency) has also conducted a series of subscale flight experiments [1–3] to acquire technologies for reentry vehicles, as shown in Fig. 1. Each system was optimized under the specified speed range of reentry flight. However, for reliability of future space transportation systems, it is necessary to operate the whole flight phase of reentry with a single configuration. One of the proposed configurations is a lifting-body type reentry vehicle, which does not have large wings unlike conventional wing-body type vehicles, and in which the fuselage itself generates lifting force. Thus, a lifting-body type configuration has good volumetric efficiency. Furthermore, it also has a good aero-heating characteristic because of its blunt nose.

Although various lifting-body type reentry vehicles have been proposed, such as the M2-F series and X-24 series [4], their aerodynamic characteristics over a wide range of flight conditions are not fully understood in comparison with those of wing-body type configurations. JAXA has conducted wind-tunnel tests with various lifting-body configurations to investigate the aerodynamic characteristics of lifting-body type reentry vehicles [5,6]. However, the baseline configuration of JAXA's lifting-body shows nonlinear lateral characteristics in the transonic speed region. As shown in Fig. 2, the lateral characteristics change drastically with increasing angle of attack. These nonlinear characteristics may cause unstable flight of the reentry vehicle. JAXA performed a experiment-based parametric study to improve the nonlinear lateral characteristics of the baseline configuration. The results of this parametric study indicated that the fin mounted on the fuselage causes unsymmetrical development of vortices and results in nonlinear lateral characteristics. An upswept upper-aft body and modification of the swept-back fin angle seemed to be effective to remedy the nonlinear characteristics of the baseline configuration. However, the parametric study did not provide an optimum configuration with good lateral characteristics.

Fig. 1 Subscale flight experiments performed at JAXA.

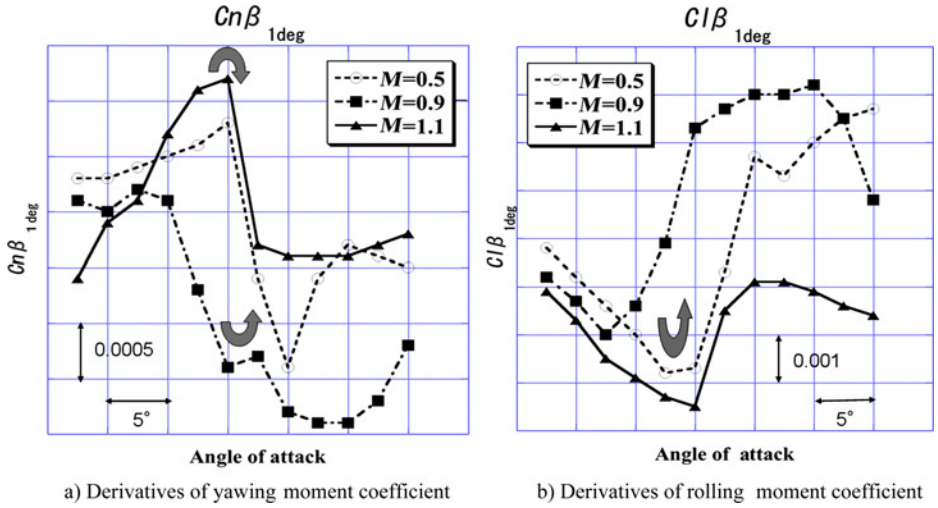

Fig. 2 Nonlinear lateral characteristics of JAXA's baseline configuration at transonic speed.

Thus, the purposes of present study were as follows: a) to investigate the causes for the nonlinear lateral characteristics of JAXA's baseline configuration by CFD (computational fluid dynamics) analysis; and b) to find the optimum configuration of lifting-body type reentry vehicle with stable lateral characteristics by using an efficient optimization algorithm.

II. Investigation of Cause for Nonlinear Lateral Characteristics

A. Baseline Configuration

The baseline configuration of JAXA's lifting-body type reentry vehicle is based on HYFLEX, which was used for a suborbital hypersonic lifting flight experiment. As shown in Fig. 3, it has a nearly triangular planform. The upper surface of the fuselage has an airfoil-like shape, while the lower surface is flat. Two outboard fins are mounted on the upper-aft region with a 20° cant angle.

B. CFD Solver and Grid

TAS (Tohoku University Aerodynamic Simulation) code [7] was used to analyze the flowfield around the lifting-body configuration. TAS code is a three-dimensional (3D) cell vertex unstructured grid-based solver. The HLLEW (Harten-Lax-van Leer-Einfeldt-Wada) method [8] was used for the numerical flux calculations. Second-order spatial accuracy was realized by a linear reconstruction of the primitive variables. LU–SGS (Lower/Upper Symmetric Gauss-Seidel) implicit method [9] was used for time integration. The Spalart–Allmaras model was adopted as a turbulence model. Figure 4 shows the computational grid around the baseline configuration. The hybrid grid, which adopted a prism layer near the wall boundary, was used. There were 35 prism layers and the total number of grid points was about 4.7 million.

C. Results

Derivatives of yawing and rolling moment coefficients were considered to evaluate the lateral characteristics. The derivatives of yawing and rolling moment coefficient used in this study were derived in the same way as in [5] for the comparison with wind tunnel test results [5]

$$Cn\beta_{1\text{deg}} = \frac{Cn\beta_{5\text{deg}} - Cn\beta_{0\text{deg}}}{5} \tag{1}$$

$$Cl\beta_{1\text{deg}} = \frac{Cl\beta_{5\text{deg}} - Cl\beta_{0\text{deg}}}{5} \tag{2}$$

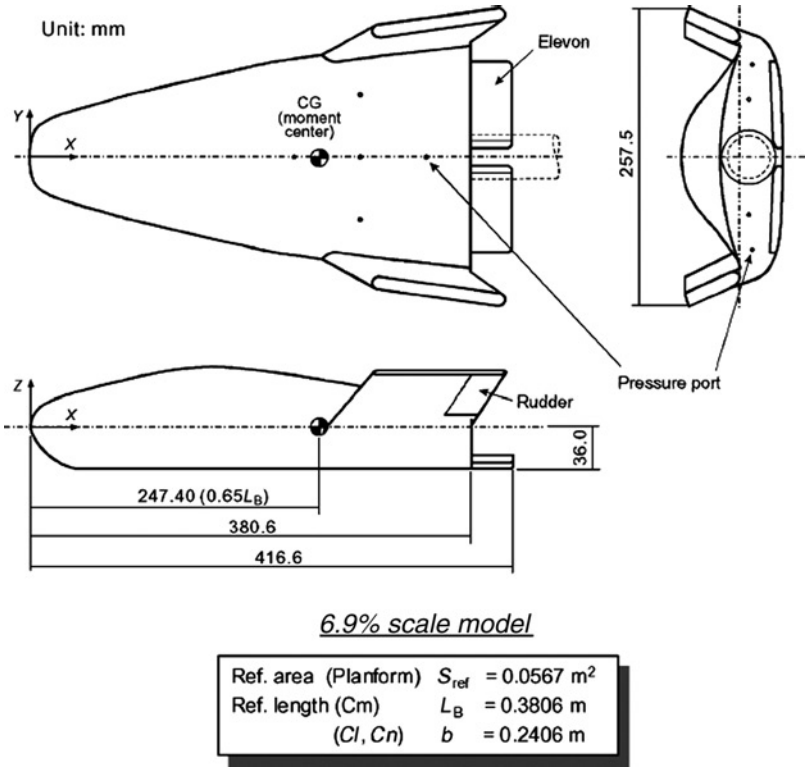

Fig. 3 Baseline configuration (6.9% scaled wind-tunnel model).

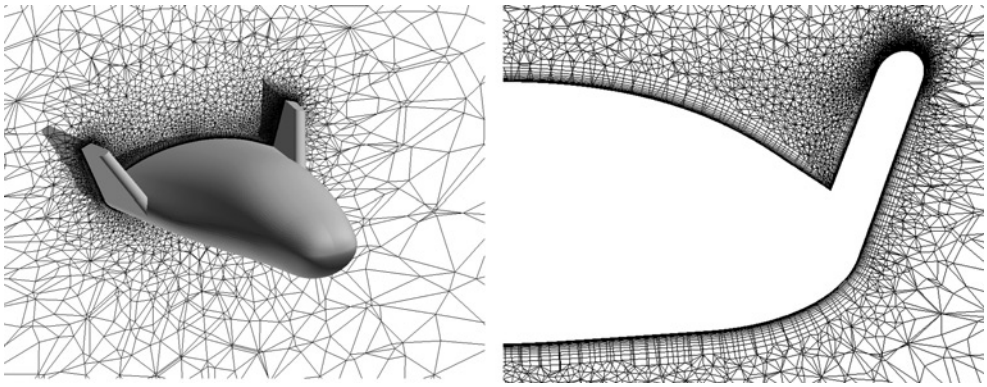

Fig. 4 Computational grid around the lifting-body.

where $Cn\beta_{0\text{deg}}(Cl\beta_{0\text{deg}})$ and $Cn\beta_{5\text{deg}}(Cl\beta_{5\text{deg}})$ are the lateral characteristic coefficients at sideslip angles of 0° and 5°, respectively.

Figure 5 shows a comparison of the CFD results with those of the wind-tunnel tests. Although the CFD results did not agree with the wind-tunnel test results, CFD analysis predicted the nonlinear lateral characteristics of JAXA's baseline configuration.

To determine the causes for the nonlinear lateral characteristics, helicity contours at three chordwise sections, surface streamline, and surface pressure distribution at $\beta = 5°$ were investigated by changing angle of attack. As shown in Fig. 6, the vortex at the right fin was stronger than that at the left fin at an angle of attack of 0°. This

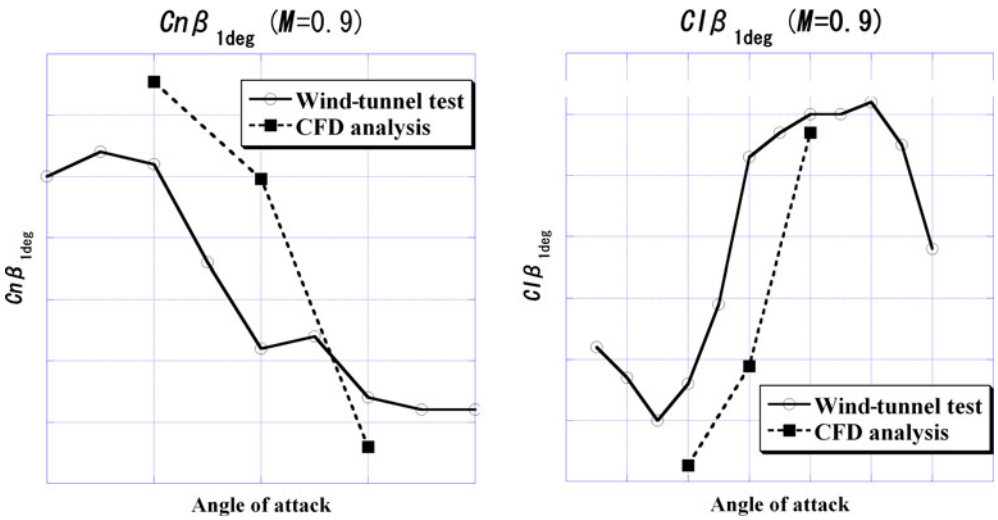

Fig. 5 Comparison of CFD and wind-tunnel test data.

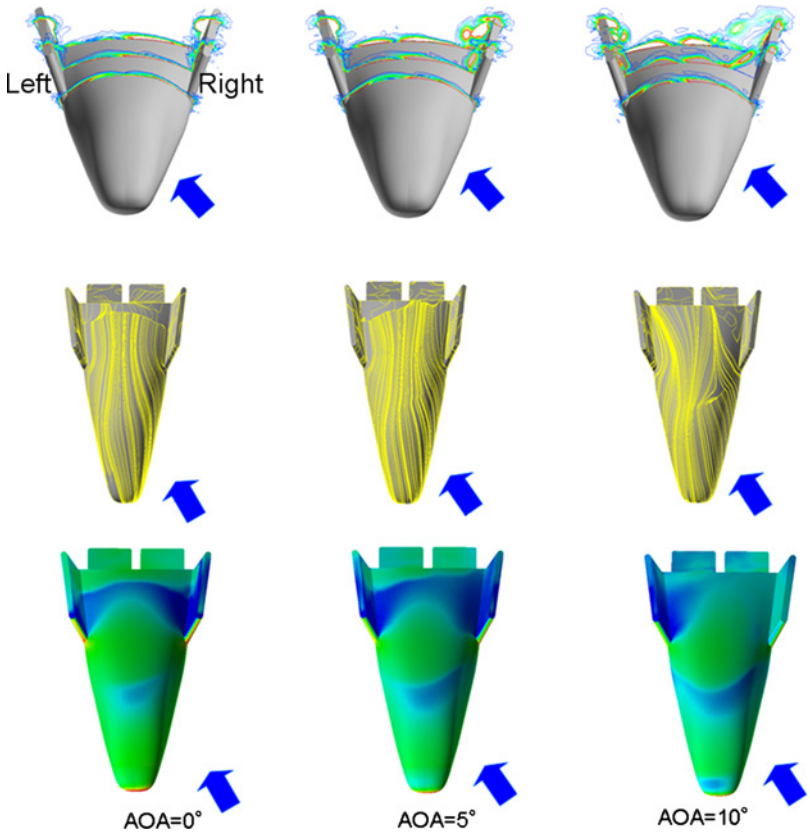

Fig. 6 Helicity contours, surface streamline, and surface pressure distribution on baseline configuration ($M = 0.9$, $\beta = 5°$).

strong vortex accelerates the flow and delays separation on the right-hand side. Thus, the low pressure region on the right-hand side is larger than that on the left-hand side. This trend becomes more marked with increasing angle of attack. However, at an angle of attack of 10°, the vortex on the right-hand side began to separate from the leading edge of the fin and broke down near the end of the fin, while the vortex on the left-hand side increased in strength and delayed separation on the left-hand side. Thus, the flow of the right-hand side separated earlier than that on the left-hand side, and the low pressure region on the left-hand side became larger than that on the right-hand side. This unsymmetrical development of vortices generated from the fins results in the nonlinear lateral characteristics of the baseline configuration of JAXA's lifting-body. It corresponds to the result of experiment conducted by JAXA [5,6].

III. Optimization to Improve Nonlinear Lateral Characteristics of Lifting-Body

A. Definition of Design Variables

JAXA performed a parametric study to improve the nonlinear lateral characteristics of the baseline configuration. According to the results of the parametric study, an upswept upper-aft body and modification of the swept-back fin angle were effective to remedy the nonlinear characteristics of the baseline configuration. Thus, only the upswept upper-aft body and modification of the swept-back fin angle were considered here. The four design variables adopted to define the upswept upper-aft and the swept-back fin angle are shown in Fig. 7: dv1–dv3 are for the upswept upper-aft and dv4 defines the swept-back fin angle.

B. Definition of Objective Function

To improve the lateral characteristics over a wide range of Mach number, the following objective functions were defined:

Minimize

$$\left.\begin{aligned} \Delta Cn\beta &= \sqrt{\Delta Cn\beta^2_{M=0.5} + \Delta Cn\beta^2_{M=0.9} + \Delta Cn\beta^2_{M=1.1}} \\ \Delta Cl\beta &= \sqrt{\Delta Cl\beta^2_{M=0.5} + \Delta Cl\beta^2_{M=0.9} + \Delta Cl\beta^2_{M=1.1}} \end{aligned}\right\} \tag{3}$$

where

$$\left.\begin{aligned} \Delta Cn\beta_{M=\text{arbitarary}} &= \sqrt{\frac{\{(A\alpha_1 + B) - Cn\beta_{1\text{deg}}(\alpha_1)\}^2 + \{(A\alpha_2 + B) - Cn\beta_{1\text{deg}}(\alpha_2)\}^2 + \{(A\alpha_3 + B) - Cn\beta_{1\text{deg}}(\alpha_3)\}}{3}} \\ \Delta Cl\beta_{M=\text{arbitarary}} &= \sqrt{\frac{\{(C\alpha_1 + D) - Cl\beta_{1\text{deg}}(\alpha_1)\}^2 + \{(C\alpha_2 + D) - Cl\beta_{1\text{deg}}(\alpha_2)\}^2 + \{(C\alpha_3 + D) - Cl\beta_{1\text{deg}}(\alpha_3)\}}{3}} \end{aligned}\right\} \tag{4}$$

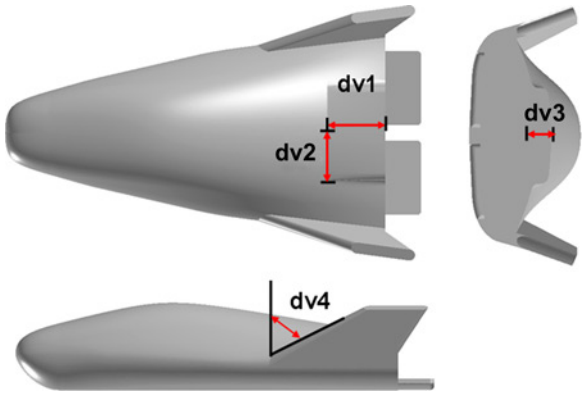

Fig. 7 Definition of design variables.

Table 1 18 computation conditions for objective functions evaluation

Mach number	Angle of attack [°]	Sideslip angle [°]	Reynolds number
0.5	0, 5, 10	0, 5	
0.9	0, 5, 10	0, 5	3.1×10^6
1.1	0, 5, 10	0, 5	

$A\alpha + B$ and $C\alpha + D$ are the least square regression lines of $Cn\beta_{1\text{deg}}(\alpha)$ and $Cl\beta_{1\text{deg}}(\alpha)$, respectively. In this study, $\alpha_1 = 0°$, $\alpha_2 = 5°$, and $\alpha_3 = 10°$. To obtain these objective functions, it requires the Navier–Stokes calculations for 18 flow conditions described in Table 1. One Navier–Stokes calculation conducted in this study takes about 10 h with 100 CPUs of an Altix 3700 at the Institute of Fluid Science, Tohoku University. Thus, the computational cost may be too high to obtain the optimum solution with conventional optimization tools, such as evolutionary algorithms. To reduce the computational time for optimization, an efficient optimization method using a response surface model was adopted here.

C. Efficient Global Optimization for Multi-Objective Problem (EGOMOP)

A response surface model methodology has been used in the engineering design field to reduce the computational time required for optimization. However, most response surface models have problems with fidelity because the estimated values contain errors. To resolve this problem, Jones et al. suggested EGO (efficient global optimization), which uses the Kriging model as a response surface model [10]. The Kriging model predicts not the function value itself but the probability distribution of the function value at an unknown point. Using the probability distribution of the function value, it is possible to predict not only the function value but also its uncertainty at the same time. In EGO, the exploration is based on the probability of being superior to the current optimum instead of the objective function value itself. In case of optimization using response surface models, a solution (point B in Fig. 8) with a large predicted function value with a large uncertainty (error) may be smaller than a solution (point A in

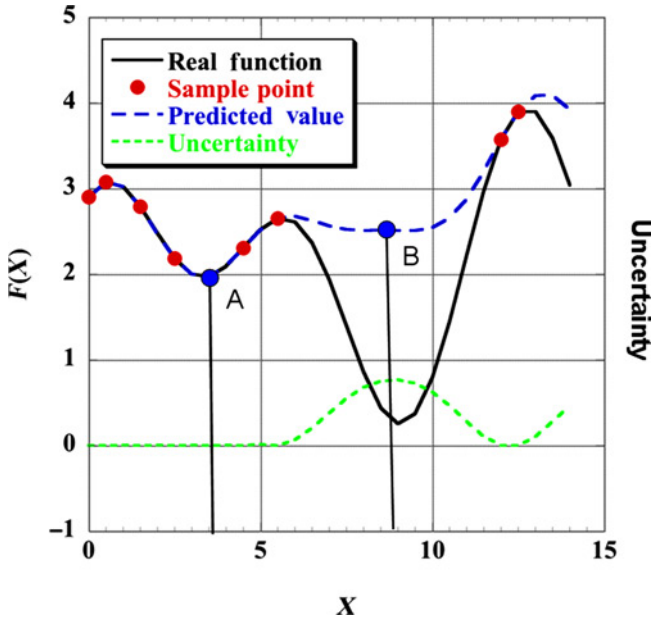

Fig. 8 Predicted value and uncertainty of response surface model.

Fig. 8) with a small predicted function value with a small uncertainty (error) as shown in Fig. 8. EGO selects the solution that has the largest probability of being superior to the current optimum as an additional sample point. This procedure makes it possible to explore a design space globally and improve the accuracy of the response surface model.

The probability of being superior to the current optimum solution is defined by the criterion of "expected improvement (EI)" as follows:

In minimization problems

$$E(I(\mathbf{x})) = (f_{\min} - \hat{y})\Phi\left(\frac{f_{\min} - \hat{y}}{s}\right) + s\phi\left(\frac{f_{\min} - \hat{y}}{s}\right) \tag{5}$$

where $\hat{y}$ and s are predicted function value and uncertainty, respectively. $f_{\min}$ is the current minimum value. Φ and ϕ are the standard distribution and normal density, respectively.

In a similar way, the probability of satisfying constraints [11]

$$c_i(\mathbf{x}) > a_i, \quad i = 1, \ldots, k \tag{6}$$

can be calculated as follows

$$P(c_i(\mathbf{x}) > a_i) = 1 - \Phi\left(\frac{\hat{c}_i - a_i}{s_i}\right), \quad i = 1, \ldots, k \tag{7}$$

where $\hat{c}_i$ and s_i are the estimated value and uncertainty of constraint function c_i, respectively.

The possibility of being superior to the current optimum subject to constraints can be derived as follows [12]

$$E(I_c(\mathbf{x})) = E(I(\mathbf{x})) \cdot P(c_i(\mathbf{x}) > a_i) \tag{8}$$

Essentially, application of EGO is limited to single objective problems. Knowles et al. suggested ParEGO (Pareto EGO) [13], which converts multiple objective functions into single objective functions by using a utility function method to extend EGO to multi-objective problems. However, its performance depends largely on the selection of weight parameters of the utility function. Jeong et al. proposed EGOMOP (EGO for multi-objective problems) [14], treating EI of each objective function as a fitness function in multi-objective genetic algorithms. Instead of finding the Pareto solutions in terms of objective functions, this method explores the Pareto solutions in terms of EIs. Among the Pareto solutions of EIs, additional sample points are selected for global exploration of the design space and improvement of Kriging models.

In this study, EGOMOP was adopted to solve the defined design problem. The procedure of EGOMOP, as shown in Fig. 9, consists of the following steps:

a) selection of initial sample points by a space filling method;
b) evaluation of initial sample points using a high-fidelity solver;
c) construction of Kriging models;
d) exploration of Pareto solutions of EIs using MOGA (Multi-Objective Genetics Algorithm) [15] coupled with Kriging models;
e) selection of additional sample points from Pareto solutions of EIs;
f) evaluation of additional sample points using a high-fidelity solver;
g) update of Kriging models.

This routine is iterated until satisfactory design results are obtained or the number of high-fidelity evaluation reaches the designated number.

D. Results

1. Design Result Without Constraints

First, EGOMOP was applied to solve the optimization problem without constraints. Ten initial sample points were selected to construct Kriging models using Latin hypercube sampling (LHS) [16]. LHS ensures that a point always exists inside the interval partitioned by the number of sample points. This makes it possible to spread sample points

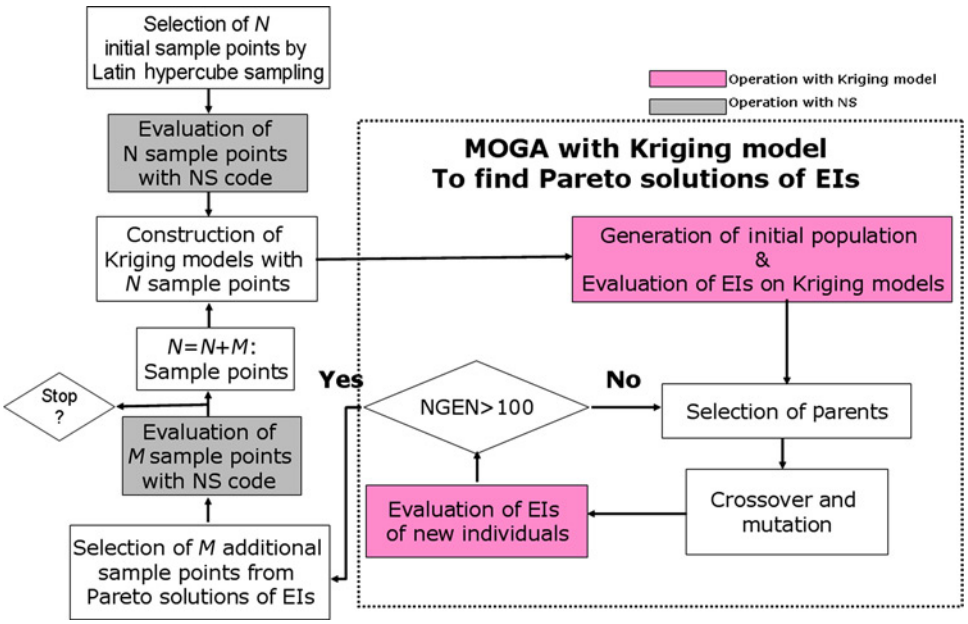

Fig. 9 Overall procedure of EGOMOP.

uniformly in the design space. As shown in Fig. 10, sample points were spread uniformly throughout the whole design space and various lifting-body configurations were generated.

The objective functions of these configurations were evaluated with the same N–S (Navier–Stokes) solver used in the previous section. With these sample points, Kriging models were constructed and the procedure described in Fig. 9 was performed. After completion of one cycle, the configuration (Opt1) outperforming all sample configurations was obtained. Figure 11 shows objective function values and configuration of the baseline, sample points, and the Opt1. Even among the sample points, several configurations had better objective function values than the baseline. Opt1 and sample points with good performance had a relatively large upswept upper-aft and swept-back fin angle.

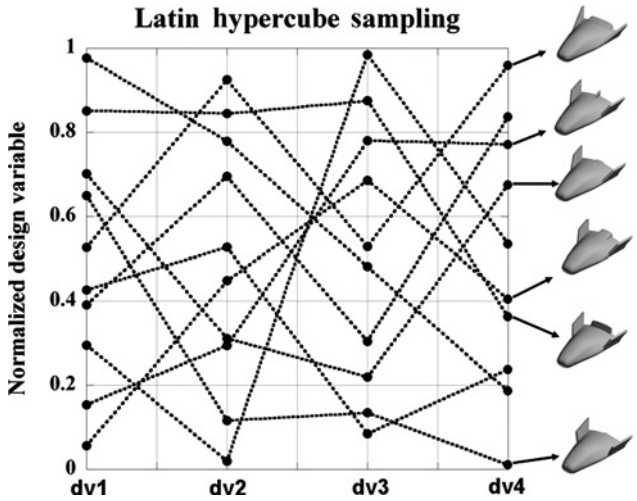

Fig. 10 Sample points for construction of Kriging models.

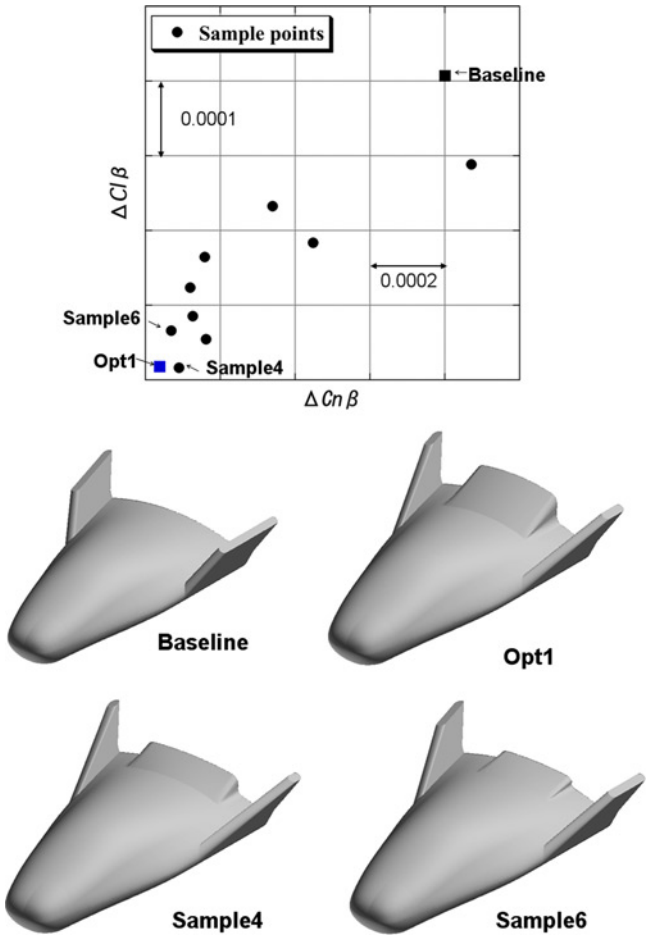

Fig. 11 Objective function values and geometry of lifting-body reentry vehicles.

Figure 12 compares $Cn\beta_{1\text{deg}}(\alpha)$ and $Cl\beta_{1\text{deg}}(\alpha)$ of the baseline configuration and those of the Opt1 configuration. While $Cn\beta_{1\text{deg}}(\alpha)$ and $Cl\beta_{1\text{deg}}(\alpha)$ of the baseline configuration changed nonlinearly as the angle of attack increased, those of Opt1 changed linearly. The helicity contours at three chordwise sections and the surface pressure distribution of Opt1 were investigated to determine the cause for this improvement. As shown in Fig. 13, the high-pressure region in the upswept upper-aft prevented the flow from accelerating or separating from the body and made it possible to have linear lateral characteristics. However, this high-pressure region degraded the L/D performance of the lifting-body. Table 2 shows the differences in L/D performance from the baseline configuration. Overall, the configurations with a large upswept upper-aft body had low L/D performance.

2. Design Result with Constraints

To improve L/D performance of the lifting-body, design was performed with L/D constraints defined as follows.

$$\left.\begin{aligned} (\mathrm{L/D})_{M=0.5,\mathrm{AOA}=0^\circ} &\geqslant (\mathrm{L/D})^{\mathrm{baseline}}_{M=0.5,\mathrm{AOA}=0^\circ} \\ (\mathrm{L/D})_{M=0.5,\mathrm{AOA}=5^\circ} &\geqslant (\mathrm{L/D})^{\mathrm{baseline}}_{M=0.5,\mathrm{AOA}=5^\circ} \\ (\mathrm{L/D})_{M=0.5,\mathrm{AOA}=10^\circ} &\geqslant (\mathrm{L/D})^{\mathrm{baseline}}_{M=0.5,\mathrm{AOA}=10^\circ} \end{aligned}\right\} \tag{9}$$

The probability of satisfying each constraint was calculated by Eq. (7) and treated as a penalty in Eq. (8). Two design cycles were performed here. Figure 14 shows the objective function values and configurations. Table 3 shows the

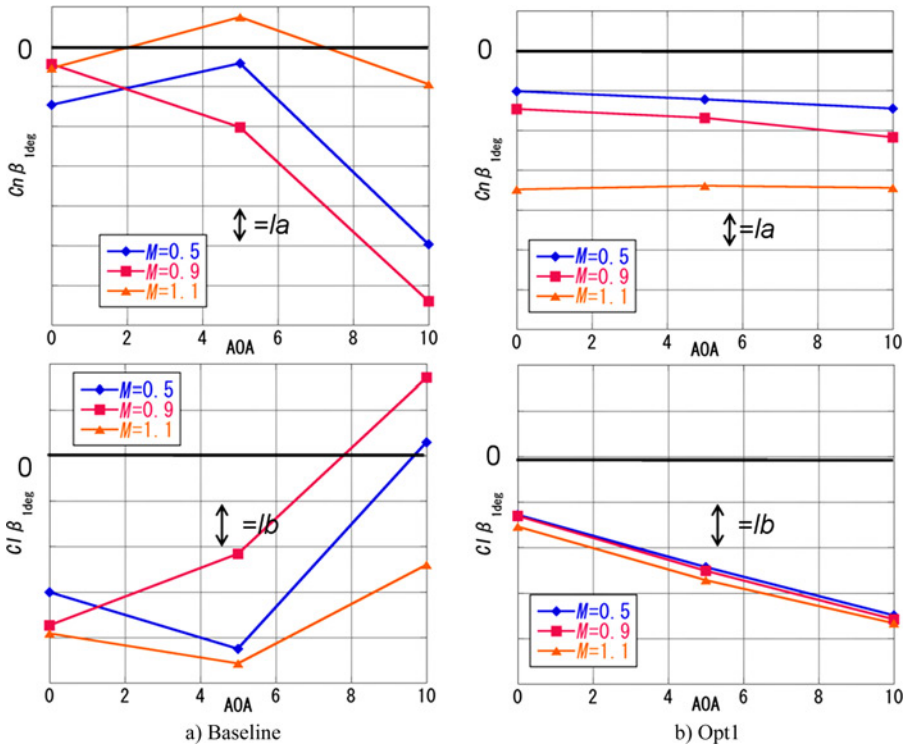

Fig. 12 $Cn\beta_{1deg}$ (α) and $Cl\beta_{1deg}$ (α).

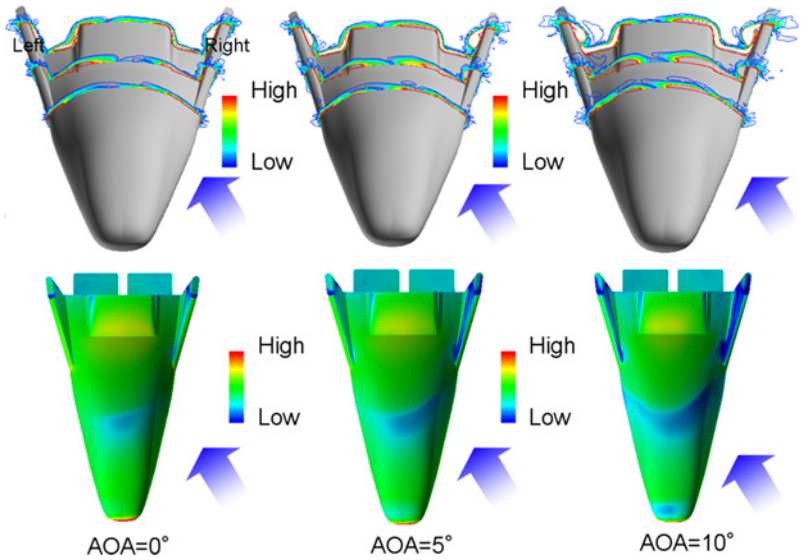

Fig. 13 Helicity contours and surface pressure distribution on Opt1 configuration ($M = 0.9$, $\beta = 5°$).

Table 2 L/D performance comparison ($M = 0.5$)

	AOA (°)		
	0	5	10
Baseline	–	–	–
Sample 4	−2.157	−1.765	−0.816
Sample 6	−1.038	−0.719	−0.123
Opt1	−2.313	−2.073	−1.149

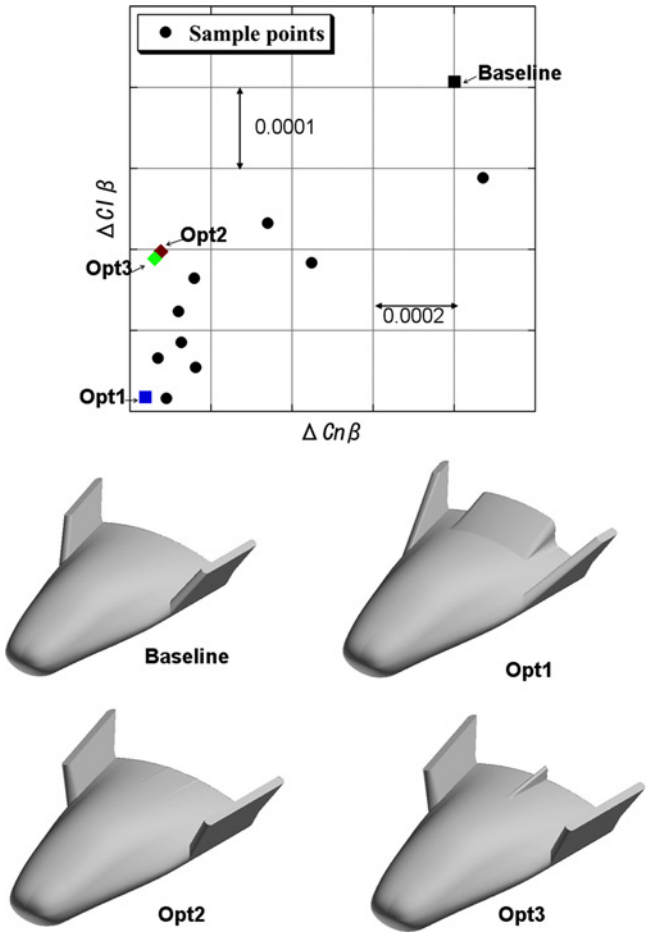

Fig. 14 Objective function values and geometry of lifting-body reentry vehicles.

L/D difference from the baseline configuration. The swept-back angle of designed configurations (Opt2 and Opt3) was almost 0° and there was a very small upswept upper-aft.

The lateral characteristics of Opt2 and Opt3 configurations were slightly poorer than those of Opt1 but were still much better than those of the baseline configuration. In terms of L/D performance, Opt2 and Opt3 were much better than Opt1 and comparable to the baseline configuration. Figure 15 shows $Cn\beta_{1\text{deg}}(\alpha)$ and $Cl\beta_{1\text{deg}}(\alpha)$ of Opt2 and Opt3 configurations.

Figure 16 shows the helicity contours at three chordwise sections and surface pressure distributions of Opt2 and Opt3. The vortex generated at the right-hand side fin separated more quickly than that at the left-hand side fin. This

Table 3 L/D performance comparison ($M = 0.5$)

	AOA (°)		
	0	5	10
Baseline	–	–	–
Opt1	−2.313	−2.073	−1.149
Opt2	−0.009	−0.095	−0.152
Opt3	−0.085	−0.162	−0.193

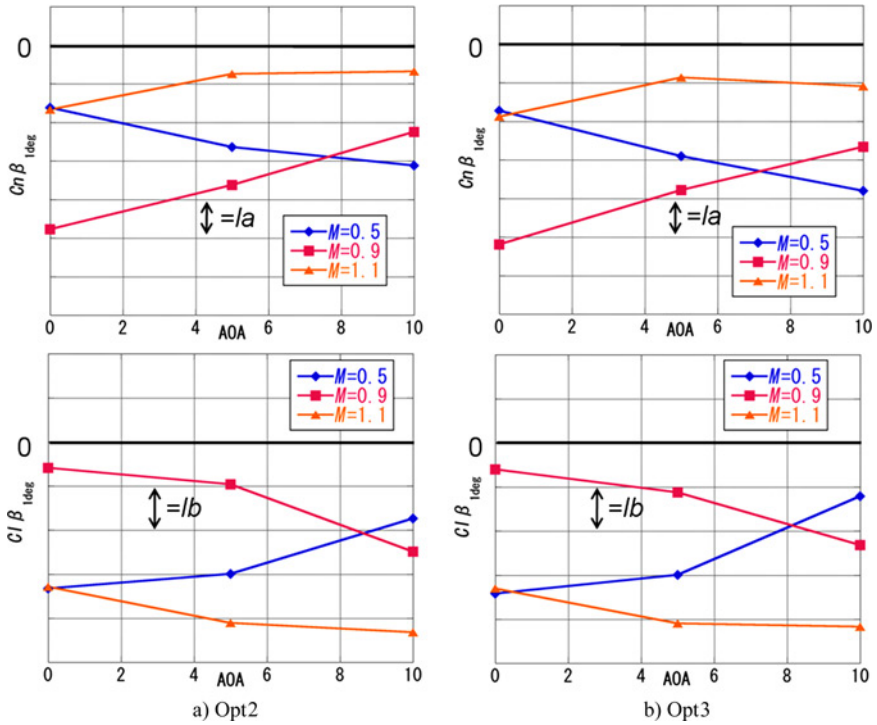

a) Opt2 b) Opt3

Fig. 15 $Cn\beta_{1deg}$ (α) and $Cl\beta_{1deg}$ (α).

trend increased with increasing angle of attack. Thus, the pressure on the left-hand side fin was lower than that on the right-hand side fin, regardless of changes in the angle of attack. This makes it possible to have linear lateral characteristics.

3. Further Investigation of the Effect of Upswept Upper-aft and Swept-back Fin Angle

The difference between Opt2 and Opt3 is in the upswept shape of the upper-aft. To investigate the effects of upswept upper-aft, two configurations were investigated here. The first was the configuration with no upsweep of the upper-aft and no swept-back fin angle (Base_fin0). The other was the configuration with the same upswept upper-aft as in Opt1 and no swept-back fin angle (Opt1_fin0). To compare the effects of a large swept-back fin angle, the configuration with the same upswept upper-aft as Opt3 and the same swept-back fin angle as Opt1 was also prepared (Opt3_finopt1). The configurations and the lateral characteristics are shown in Fig. 17. Base_fin0 showed almost the same lateral performance as Opt2 and Opt3. L/D performance was also the same as for Opt2 and Opt3, as shown in Table 4. This meant that the small upswept upper-aft of Opt2 and Opt3 yielded little influence on improvement of aerodynamic characteristics.

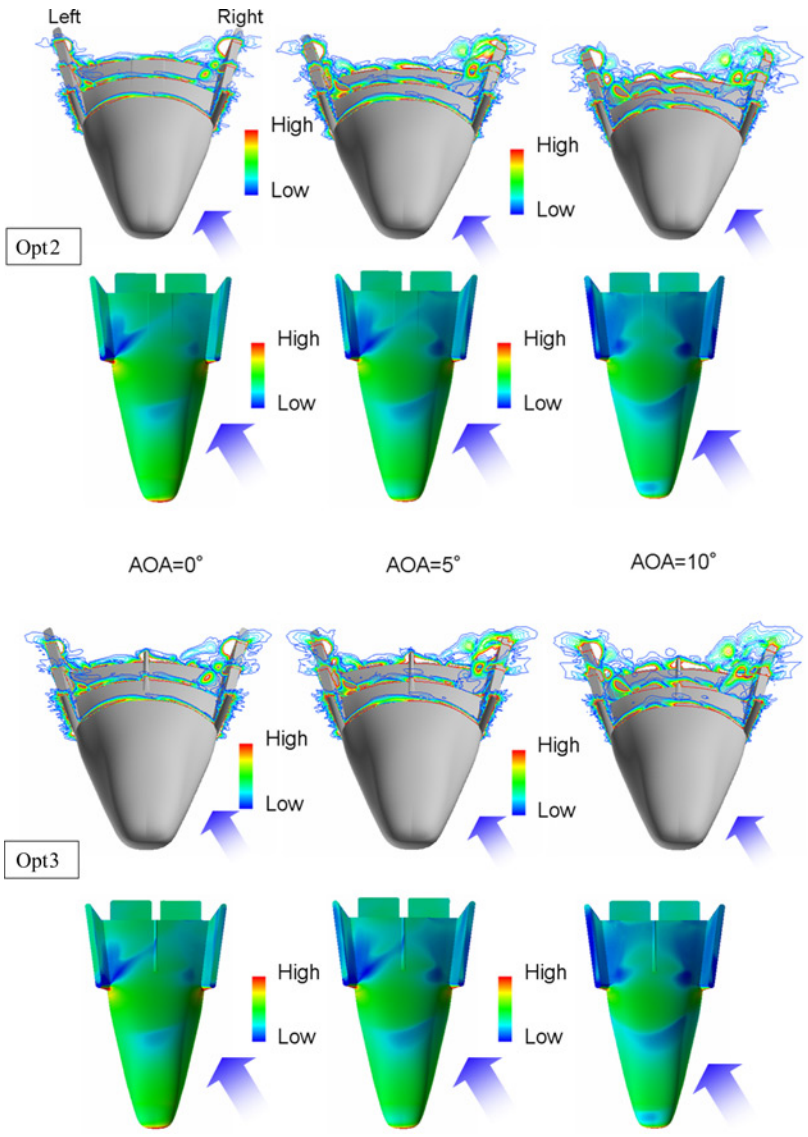

Fig. 16 Helicity contours and surface pressure distribution on Opt2 and Opt3 configuration ($M = 0.9$, $\beta = 5°$).

In the case of Opt1_fin0, although $\Delta Cn\beta$ was similar to that of Base_fin0, $\Delta Cl\beta$ was improved. Figure 18 shows the helicity contours at three chordwise sections and surface pressure distribution on Opt1_fin0. In contrast to Opt2 and Opt3, the vortex generated from the leading edge of the fin does not separate rapidly despite the increase in angle of attack because the high-pressure region caused by the large upswept upper-aft prevents flow separation. Thus, the pressure on the right-hand side fin remains lower than that on the left-hand side fin and linear lateral characteristics are preserved. However, similar to Opt1, the large upswept upper-aft causes degradation of the L/D performance.

In the case of Opt3_finopt1, $\Delta Cl\beta$ is better than that of Opt1_fin0 and L/D performance is comparable to that of Base_fin0. As shown in Fig. 19, the vortex generated from the fin accelerates the flow near the fin with increasing angle of attack. The pressure on the right-hand side fin is weaker than that on the left-hand side at all angles of attack, and thus linear lateral characteristics can be achieved. Figure 20 shows $Cn\beta_{1\text{deg}}(\alpha)$ and $Cl\beta_{1\text{deg}}(\alpha)$. In contrast to the other configurations, the lateral characteristics were not so sensitive to Mach number. This feature would be preferable from the standpoint of control.

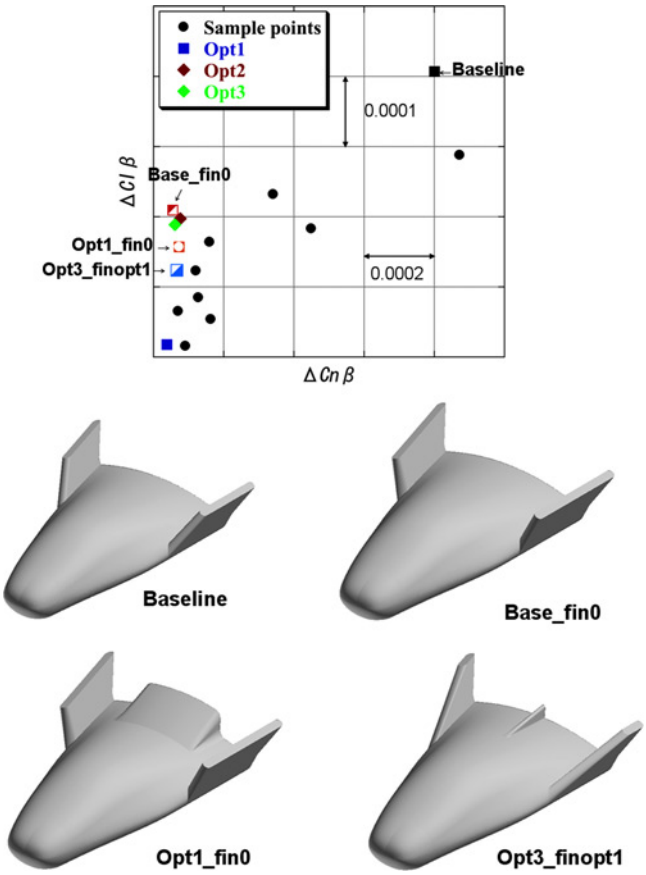

Fig. 17 Objective function values and geometry of lifting-body reentry vehicles.

Table 4 L/D performance comparison ($M = 0.5$)

	AOA (°)		
	0	5	10
Baseline	–	–	–
Base_fin0	−0.009	−0.104	−0.153
Opt1_fin0	−2.096	−1.771	−0.944
Opt3_finopt1	−0.447	0.298	0.123

IV. Conclusions

This study was performed to improve the nonlinear lateral characteristics of a lifting-body type reentry vehicle. First, the causes for the nonlinear lateral characteristics of JAXA's baseline configuration were investigated by CFD analysis. The results indicated that fins mounted on JAXA's baseline lifting-body configuration cause unsymmetrical development of vortices and result in nonlinear lateral characteristics.

EGOMOP was adopted here for efficient design optimization. EGOMOP predicts potential optimum solutions based on the probability estimated by the Kriging model. A solution with a poor predicted function value with a large degree of uncertainty (error) may be more promising than a solution with a good predicted function value with a small degree of uncertainty (error). EGOMOP makes it possible to explore a design space globally and improve the accuracy of the response surface model. Use of the Kriging model markedly reduced the computational time for optimization. The optimization without L/D constraints produced a configuration with large upswept upper-aft and

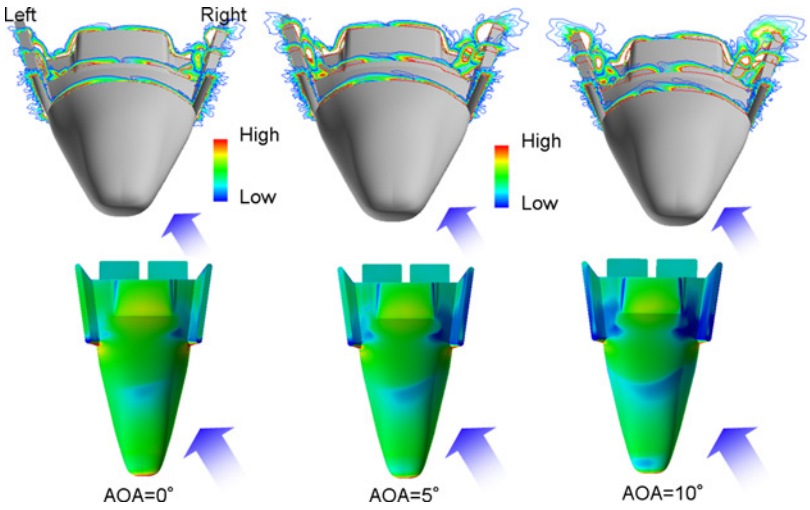

Fig. 18 Helicity contours and surface pressure distribution on Opt1_fin0 configuration ($M = 0.9$, $\beta = 5°$).

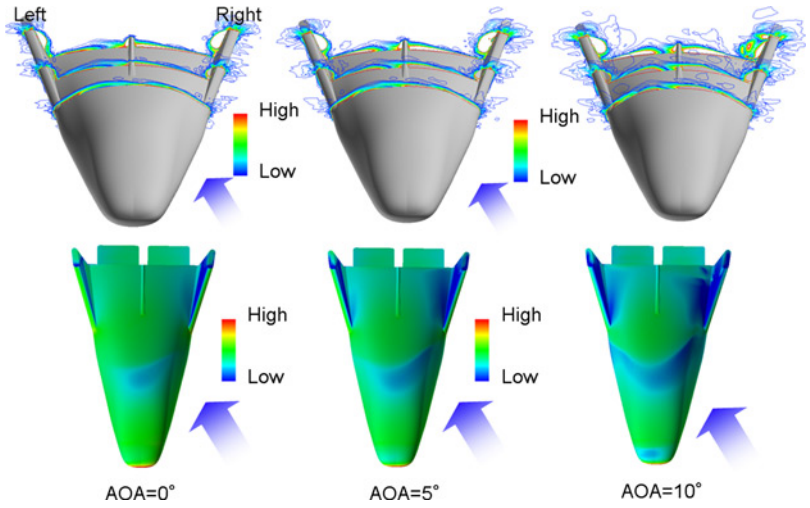

Fig. 19 Helicity contours and surface pressure distribution on Opt3_finopt1 configuration ($M = 0.9$, $\beta = 5°$).

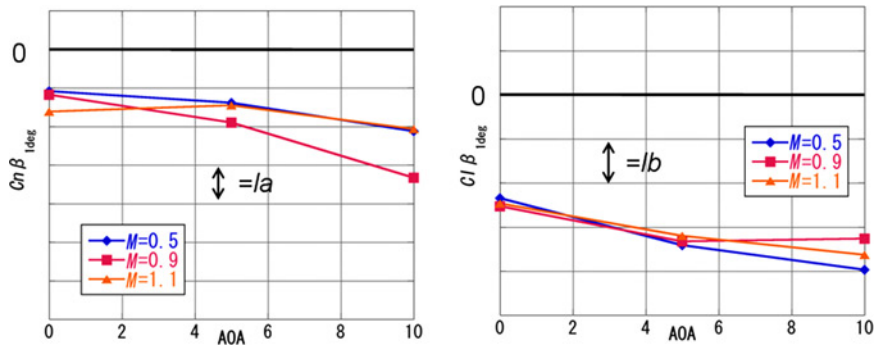

Fig. 20 $Cn\beta_{1deg}$ (α) and $Cl\beta_{1deg}$ (α).

large swept-back fin angle. This design showed the best lateral characteristics. However, its L/D performance was much lower than that of the baseline configuration. Optimization with L/D constraints was also performed. In this optimization, configurations with small upswept upper-aft and no swept-back fin angle were generated. Although the lateral characteristics of these configurations were slightly poorer than those of the unconstrained optimum design, their L/D performance was comparable to that of the baseline configuration. Further investigations were also performed to determine the effects of the upswept upper-aft and the swept-back fin angle. The results indicated that a large swept-back fin angle is very effective for both lateral characteristics and L/D performance, while the upswept upper-aft is effective only on the lateral characteristics of the lifting-body type reentry vehicle.

References

[1] Akimoto, T., Ito, T., Yamamoto, M., Bando, T., and Inoue Y., "Orbital Re-entry Experiment (OREX) — First Step of Space Return Flight Demonstrations in Japan," IAF-94-V.2.525, 1994.

[2] Shirouzu, M., and Yamamoto, M., "Overview of the HYFLEX Project," AIAA Paper 96-4524, 1996.

[3] Nakayasu, H., and Nagayasu, M., "On the Automatic Landing Flight Experiment (ALFLEX)," NAL SP-39T, 1998.

[4] Barret, C., "The Lifting Body Legacy—X-33", *37th AIAA Aerospace Sciences Meeting and Exhibit*, Reno, NV, 11–14 January 1999, AIAA, Reston, VA, AIAA Paper 99-0382.

[5] Kawato, H., Watanabe, S., Yamamoto, Y., and Fujii K., "Aerodynamic Performances of Lifting-Body Configurations for Reentry Vehicle," *Journal of Spacecraft and Rockets*, Vol. 42, 2005, pp. 232–239.
doi: 10.2514/1.2418

[6] Kurita, M., Nakakita, K., Mitsuo, K., and Kawato, H., "Aerodynamic Characteristics of a Lifting-Body-Type Reentry Vehicle at Transonic Speeds", *44th AIAA Aerospace Sciences Meeting and Exhibit*, Reno, NV, 9–12 January 2006, AIAA, Reston, VA, AIAA Paper 2006-665.

[7] Nakahashi, K., Togashi, F., Fujita, T., and Ito, Y., "Numerical Simulations on Separation of Scaled Supersonic Experimental Airplane from Rocket Booster at Supersonic Speed", *32nd AIAA Fluid Dynamics Conference and Exhibit*, 24–26 June 2002, St. Louis, MS, AIAA, Reston, VA, AIAA Paper 2002-2843.

[8] Obayashi, S., and Guruswamy, G. P., "Convergence Acceleration of an Aeroelastic Navier-Stokes Solver," *AIAA Journal*, Vol. 33, No. 6, 1995, pp. 1134–1141.
doi: 10.2514/3.12533

[9] Sharov, D., and Nakahashi, K., "Reordering of Hybrid Unstructured Grids for Lower-Upper Symmetric Gauss-Seidel Computations," *AIAA Journal*, Vol. 36, No. 3, 1998, pp. 484–486.
doi: 10.2514/2.392

[10] Jones, D. R., Schonlau, M., and Welch, W. J., "Efficient Global Optimization of Expensive Black-Box Function," *Journal of Global Optimization*, Vol. 13, 1998, pp. 455–492.

[11] Matthias, S., "Computer Experiments and Global Optimization," Ph.D Dissertation, Statistics and Actuarial Science Department, University of Waterloo, Waterloo, Ontario, 1997.

[12] Jeong, S., Obayashi, S., and Yamamoto, K., "A Kriging-based Probabilistic Optimization Method with an Adaptive Search Region," *Engineering Optimization*, Vol. 38, 2006, pp. 541–555.
doi: 10.1080/03052150600627073

[13] Knowles, J., and Hughes, E. J., "Multiobjective Optimization on a Budget of 250 Evaluation," *Proceedings of the Third International Conference of EMO 2005*, Springer, 2005, pp. 176–190.

[14] Jeong, S., Minemura, Y., and Obayashi, S., "Optimization of Combustion Chamber for Diesel Engine Using Kriging Model," *Journal of Fluid Science and Technology*, Vol. 1, 2006, pp. 138–146.
doi: 10.1299/jfst.1.138

[15] Sasaki, D., and Obayashi, S., "Efficient Search for Trade-Offs by Adaptive Range Multi-Objective Genetic Algorithms," *Journal of Aerospace Computing, Information, and Communication*, Vol. 2, No. 1, 2005, pp. 44–64.
doi: 10.2514/1.12909

[16] McKay, M. D., Beckman, R. J., and Conover, W. J., "A Comparison of Three Methods for Selecting Values of Input Variables in the Analysis of Output from a Computer Code," *Technometric*, Vol. 21, 1979, pp. 239–245.
doi: 10.2307/1268522

K. Cohen
Associate Editor